Graveyard orbits for future Mars missions

Aggarwal, Kapish; Noomen, Ron

DOI
10.1016/j.asr.2022.07.023

Publication date
2023

Document Version
Final published version

Published in
Advances in Space Research

Citation (APA)
Aggarwal, K., & Noomen, R. (2023). Graveyard orbits for future Mars missions. *Advances in Space Research*, *72*(7), 2901-2916. https://doi.org/10.1016/j.asr.2022.07.023

Available online at www.sciencedirect.com

ScienceDirect

Advances in Space Research 72 (2023) 2901–2916

ADVANCES IN SPACE RESEARCH (a COSPAR publication)

www.elsevier.com/locate/asr

Graveyard orbits for future Mars missions

Kapish Aggarwal *, Ron Noomen

Faculty of Aerospace Engineering, Delft University of Technology, Kluyverweg 1, 2629 HS Delft, the Netherlands

Received 16 February 2022; received in revised form 4 July 2022; accepted 10 July 2022
Available online 16 July 2022

Abstract

Mars is expected to become a focal point of exploration (human and robotic) in the coming century, with a very likely need for a robust space infrastructure. Be it communication and navigation satellite constellations or scientific missions in low Mars orbits (LMO) and Areosynchronous orbits (ASO), every individual satellite will have a definitive period of operation after which it becomes derelict. At the end-of-life (EOL) the satellite shall be proactively dealt with in a sustainable manner to protect our access to the space environment of Mars and opportunities to use this. Clearly, impacting Mars or escaping Mars' gravity are no viable options. This paper aims at identifying graveyard orbit solutions in circummartian space for future Mars space debris. Orbital stability for a period of 200 years is studied for Martian orbits using the symplectic integration technique. Extensive validations are performed and propagation and integration settings are tuned to suit a variety of configurations. A plethora of candidate graveyard orbit solutions are found and presented for orbits in the ASO and LMO regimes. For example, it is found that transferring an ASO satellite to 400 km below the nominal orbit altitude would ensure a stability margin of ±25 km for at least 200 years. Multiple orbital geometry characteristics (combinations of semi-major axis, inclination, right ascension of ascending node), satellite geometries (various values of area-to-mass ratio) and uncertainties are studied to produce a comprehensive analysis of long-term stability of potential graveyard orbits around Mars, making them attractive for such purposes. The protected zones are found to be safe from debris even for an uncertainty in initial eccentricity of 0.01 and variations in cross-sectional area due to uncontrolled tumbling. The overall objective of this paper is to make designers of future missions to Mars aware of the EOL aspects and include this in their mission design proposals at an early stage already.

Keywords: End-of-life; Mars; Space debris; Graveyard orbits; Long-term stability

1. Introduction

With governments and private entities pouring in resources for human and robotic exploration of Mars, it is envisaged that constellations of satellites for navigation, network connectivity etc. would soon be required in orbits around Mars (Kelly and Bevilacqua, 2018; Buinhas et al., 2019). Multiple colonization plans suggest a permanent human presence on Mars from as early as the year 2030 onwards (Brueck, 2018; Drake, 2016; Hall, 2020; Knapton, 2015; SpaceX, 2019; Wall, 2020). A space infrastructure would have to co-exist which will consequently produce space debris, yet no plans for disposal of space debris exist. Thus, our access to Mars and usage of its space environment will depend on how sustainable we make our space activities. It will depend on how prudent we are in applying the lessons learnt from Earth's space debris problem to Mars.

Due to the absence of an effective natural sink mechanism on Mars, such as an atmosphere, there is a clear need to address disposal methods for future derelict satellites in Martian orbits, so that we can avoid the problems on and around Mars which we are facing in terrestrial orbits. In view of the small size of the planet along with no existing

* Corresponding author.
E-mail addresses: kapishaggarwal@yahoo.com (K. Aggarwal), R.Noomen@tudelft.nl(R. Noomen).

https://doi.org/10.1016/j.asr.2022.07.023
0273-1177/

(Suchantke et al., 2019) and foreseen debris tracking capabilities in the near future, the issue is even more acute. If this remains the case even when there exist hundreds of satellites around the planet, safe entry into Mars' orbital environment could become intricate. This also holds for the usage of the most attractive orbits around Mars. There is an urgent need to develop strategies today for disposal of spacecraft around Mars, to preserve human access to the scientific knowledge, resources, which the planet has to offer, and protect future human colonies on its surface. With huge financial investments involved in Mars missions, collisions with operational space resources could induce loss of governmental, commercial and public interest in the planet's exploration and habitation efforts. Addressing this space debris problem early on is utterly important. This study is an effort to fulfill our responsibility of long-term sustainable usage of space. To quote a recent United Nations report (United Nations, 2019): "The long-term sustainability of outer space activities is [...] the ability to maintain [...] space activities indefinitely into the future [...], in order to meet the needs of the present generations while preserving the outer space environment for future generations." Obviously, this implicitly addresses the situation around Mars as well.

This research is a feasibility study: the objective is to investigate the existence, accessibility and long-term stability of potential graveyard orbits around Mars. It is aimed at producing a variety of graveyard orbit options for (near-) future Mars satellite operators and regulators to select from, based on a trade-off of propellant requirements and stability. The nominal orbits analysed are limited to those in the areosynchronous and low-altitude regimes, as these are foreseen to host the far majority of operational spacecraft. State propagation is performed using non-averaged equations of motion in combination with a symplectic integration technique. The effects of multiple parameters (altitude, inclination, area-to-mass ratio, etc.) are analysed, and the causes of peculiarities in stability trends are identified. A comprehensive sensitivity analysis is also performed to test the robustness of the solutions found. The essence of the problem is not unfamiliar; it has been studied by other authors already (Alessi et al., 2016; Alessi et al., 2018; Domínguez-González et al., 2013; Gkolias and Colombo, 2019). Here, the problem is investigated around a new central body, with a unique environment and unknown options for EOL measures.

2. Background

2.1. Study cases

To restrict this study to the most realistic risk domain, i.e. the most popular regions in Martian orbits, it is imperative to understand the orbital characteristics of current and future artificial satellites around Mars.

Past, current and upcoming Mars orbiters chiefly use inclined elliptic orbits with many having an eccentricity as high as 0.8 and inclinations ranging from 35° to 90° (Fig. 1) (ESA, 2019; Suchantke et al., 2019). Their trajectories cross the areosynchronous orbit (ASO) altitude in the majority of cases, with apoareion altitudes mostly beyond Phobos' altitude and in some cases beyond Deimos' as well, while 400 and 1000 km are dominant periareion altitudes. Few orbiters, such as *Mars Odyssey* and *ExoMars TGO*, preferred a Sun-synchronous orbit configuration (i.e. low-altitude circular orbits with $i \approx 90°$) for science and relay purposes.

Apart from the single-spacecraft missions discussed above, a number of constellations of satellites has been proposed. Constellations, forming a network of a large number of satellites, have wide-ranging applications including navigation, telecommunication, remote sensing, geodesy etc. and, with the advent of advances in small-satellite engineering, are foreseen to be the major source of debris in circummartian space. Fig. 2 presents the altitude-inclination characteristics of 13 navigation constellation designs (consisting of a total of 120 satellites) as proposed by Bell et al. (2000), Buinhas et al. (2019), O'Keefe et al. (2005), Kelly and Bevilacqua (2018), Kuo (2000), Menggen et al. (2014) and Tingting et al. (2009). Unlike Earth's navigation constellations, a large amount of clustering can be observed near ASO altitude for 0° and 45° inclined orbits, low-altitude Sun-synchronous (near-polar) orbits, and low-altitude near-equatorial orbits. For Mars, low altitudes seem to dominate for navigation constellations. It should be noted that low-altitude satellites could also be used for remote-sensing and observation purposes as LEO satellites are used for Earth.

From the discussion above, it is concluded that the following types of orbits are expected to be most used in the future, for which EOL strategies are investigated and designed in this paper: areostationary orbits (AEO) (ASO 0), areosynchronous orbits with 45° inclination (ASO 45), low Mars orbits (LMO) with 0° inclination (LMO 0) and low Mars orbits with 90° inclination (LMO 90). It should be noted that erratic and (almost) uncontrollable debris due to spent rocket stages, ascent rockets, heat shields,

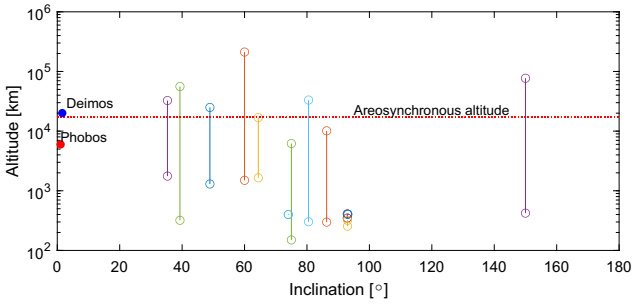

Fig. 1. Altitude-inclination characteristics of past Mars orbiter missions.

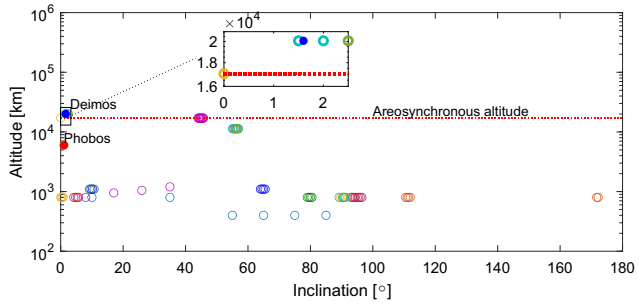

Fig. 2. Altitude-inclination characteristics of proposed Mars constellations.

etc. would also become (very) common in Martian orbits, but these are not studied here.

2.2. ΔV considerations

An elemental knowledge of the ΔV requirements and availabilities for future Martian satellites at EOL is crucial for the design of EOL strategies for obvious reasons.

Using the very common two-burn Hohmann transfer maneuver, ΔV requirements for various EOL options, for LMO and ASO cases, were calculated. Re-orbiting LMO satellites, with the original altitude being less than 800 km, to circular orbits at +100 and +500 km from the nominal altitude requires about 45 and 200 m/s of ΔV, respectively. For ASO satellites, these values are in the order of 4 and 18 m/s, respectively. De-orbiting to 50 km altitude, after which atmospheric drag is expected to take over the dynamics, requires a much greater amount of energy. For an initial 400 km altitude orbit, this would impose a ΔV requirement of 80 m/s at EOL and double the value if the nominal altitude were 800 km. On the other hand, de-orbiting from ASO altitude would require an impractical ΔV of 670 m/s. For the sake of completeness, ΔV values required for the EOL option of escape from the planet's gravity well were also computed and found to be 600 m/s for ASO and near to 1400 m/s for LMO satellites.

Thus, from the mechanical-energy perspective, escape is not a feasible EOL option for any of the orbital regimes. De-orbit is absolutely non-viable for spacecraft in the ASO regime. This is re-iterated in the following paragraph, where ΔV availability at EOL is discussed. For LMO, both de-orbiting and re-orbiting are viable from a ΔV perspective. However, knowing that Mars has no oceans, where a large space debris object could be allowed to crash, makes de-orbit an unattractive option. Also, since the average density of Mars' atmosphere is about two orders of magnitude lower than Earth's, little-to-no burning-up due to aerodynamic heating is expected. It would be highly undesirable to let a large uncontrolled satellite plunge on the solid surface, where infrastructure (or even human/robot colonies) could be present at any location in the future. Thus, re-orbiting satellites to suitable graveyard orbits is the only acceptable, realistic EOL strategy studied in this paper for the cases defined in the previous subsection.

As for the total ΔV available for Mars spacecraft, past missions show a variety of values. For example, *Mars Cube One* CubeSats carried 40 m/s (Spaceflight101, 2019), whereas *Mars Reconnaissance Orbiter (MRO)* had 754 m/s ΔV (JPL, 2006b). Some spacecraft operators also specify the excess ΔV for mission extension, which can be taken as a good estimate for the amount of ΔV available at EOL. For example, ISRO (2017) specifies that the total mission ΔV for *Mars Orbiter Mission* was 292 m/s, which included 117.4 m/s as excess for mission extension. Based on these data, it is reasonable to assume that for future missions, the maximum ΔV available for EOL maneuvers would not exceed 150 m/s, at least in the coming 20–30 years. This value is used later in this paper to limit the candidates for in-depth investigation.

3. Methodology

The basic objective is to identify graveyard orbits for human-made Mars satellites, such that they are stable for 200 years starting from the year 2050. Such a duration is a good approximation of 'forever', and is sufficient to identify, understand and extrapolate trends (Allan et al., 1964; Jacobson and Lainey, 2014; Jenkin et al., 2021). For this purpose, the maximum variation of graveyard orbit altitude w.r.t. the nominal (i.e. original) altitude is taken to be the measure of stability. The software used for the simulations is Tudat (TU Delft Astrodynamics Toolbox) (Tudat, 2018). It is a powerful open-source software for research in astrodynamics and comes with a collection of models and mathematical tools written in C++ at Delft University of Technology. The following subsections further elaborate the methodology.

3.1. Reference frames

The *MARSIAU* reference frame (Lyons and Vaughn, 1999; Semenov, 2017) is used for simulations in this project. Here, the X-axis is parallel to the IAU vector, which is a vector directed from Mars' center of mass towards the point of intersection of Earth's and Mars' mean equators at epoch J2000. The Z-axis is perpendicular to the reference plane, and the Y-axis completes the right-handed system.

3.2. Force model

This subsection includes brief descriptions of and equations for the various force model elements relevant for this paper.

3.2.1. Mars' gravity field

The gravitational potential for Mars U_{areopot} is given by (Montenbruck and Gill, 2000; Wakker, 2015):

$$U_{\text{areopot}} = -\frac{\mu}{r}\left[\sum_{n=0}^{\infty}\sum_{m=0}^{n}\left(\frac{R_{\mathcal{J}}}{r}\right)^{n} P_{nm}(\sin\phi)(C_{nm}\cos m\lambda + S_{nm}\sin m\lambda)\right] \tag{1}$$

where $\mu = Gm_{\mathcal{J}}, G = 6.67259 * 10^{-11}\ \text{m}^3/\text{kg}\,\text{s}^2$ is the universal gravitational constant, $m_{\mathcal{J}} = 6.41803584 * 10^{23}$ kg is the mass of Mars, r is the distance of the satellite from Mars' center of mass, $R_{\mathcal{J}} = 3389.5$ km is the mean equatorial radius of Mars, $P_{nm}(\sin\phi)$ are the associated Legendre functions of the first kind of degree n and order m, ϕ is the latitude, λ is the longitude and C_{nm} and S_{nm} are the gravity field harmonic coefficients (Stokes' coefficients) (Zuber, 2008). The maximum degree and order of the gravity field actually used will be discussed later.

3.2.2. Third-body perturbations

The Martian orbital third-body environment is highly dynamic due to gravitational attraction from the Sun, Phobos, Deimos, Jupiter, Earth, etc. and the objects in asteroid belts. The gravitational potential due to third-body perturbations $U_{3^{\text{rd}}-\text{body}}$ is defined as (Wakker, 2015):

$$U_{3^{\text{rd}}-\text{body}} = -\sum_i \mu_i\left[\frac{1}{|\mathbf{r}-\mathbf{r}_i|} - \frac{\mathbf{r}\cdot\mathbf{r}_i}{|r_i|^3}\right] \tag{2}$$

where i represents the i$^{\text{th}}$ perturbing body, μ_i is its gravitational parameter, $\mathbf{r}_i$ is its position vector w.r.t. Mars' center of mass, and $r_i = |\mathbf{r}_i|$. The decision regarding the inclusion of various third bodies in the simulations will be discussed later.

3.2.3. Solar radiation pressure

Inclusion of direct solar radiation pressure (SRP) is very important for accurate long-term prediction of space-debris trajectories, especially for objects with high area-to-mass ratios (Hubaux et al., 2012). The SRP perturbing potential U_{SRP} is given by (Wakker, 2015):

$$U_{\text{SRP}} = -\beta\frac{1}{|\mathbf{r}_{\odot}-\mathbf{r}|} \tag{3}$$

where $\beta = C_R\frac{A}{m}P_{\phi}$ is the solar radiation parameter, $C_R = 1+\rho$ is the coefficient of reflectivity, ρ is the effective reflectance of the satellite, A is its effective cross-sectional area, m is its mass, P_{ϕ} is the solar radiation constant which is approximately equal to $10^{17}\ \text{kg}\,\text{m/s}^2$ and $\mathbf{r}_{\odot}$ is the position vector of the Sun w.r.t. the center of mass of Mars. A conical shadow model (Hubaux et al., 2012), assuming a spherically shaped planet, is used for high accuracy.

The area-to-mass ratio (A/m) is a crucial parameter for analysing the effects of SRP. For long-term propagation of GNSS satellites in terrestrial orbits, Pardini and Anselmo (2012) used 0.01 m^2/kg. A very high value of 1 m^2/kg was also used by researchers like Anselmo and Pardini (2010) and Rosengren et al. (2019) for debris created due to breakup or surface degradation of satellites and with the prospect of a futuristic *SRP augmenting device* (assumed to be deployed during mission operations), respectively. Moreover, Suchantke et al. (2019) found that the past Martian satellites' area-to-mass ratio ranged from 0.002 to 0.04 m^2/kg, while the majority of them had a value of 0.02 m^2/kg. Also, CubeSats, which can be expected to be prominent in Martian satellite constellations, typically have an A/m value of 0.01 m^2/kg (Johnson and Engelhardt, 2018). Thus, to cater to all classes of debris and understand the effects of C_RA/m, three SRP cases, with A/m values of 0.01, 0.1 and 1 m^2/kg, are studied. C_R is chosen to be 1.3, which is a typical value for real satellites.

3.2.4. Atmospheric drag

The aerodynamic drag is modelled using the widely used equation (Wakker, 2015):

$$\mathbf{a}_{\text{drag}} = -C_D\frac{1}{2}\rho\frac{A}{m}|\mathbf{v}|\mathbf{v} \tag{4}$$

where C_D is the drag coefficient, ρ is the atmospheric density and $\mathbf{v}$ is the velocity of the satellite relative to the (co-rotating) Mars' atmosphere.

50 km altitude is chosen as termination condition for the simulations; the Mars Climate Database's (MCD) mean tabulated atmosphere used here is limited to this altitude, and the behaviour below this altitude is beyond the scope. The value for C_D used here for all simulations is 2.3, which is typical for astrodynamics simulations, along with the A/m values mentioned previously.

3.2.5. Relativity

To check for the relevance of Einstein's theory of general relativity for long-term orbit propagations around Mars, a relativistic correction needs to be introduced in the acceleration model. Such a correction takes into account both the curvature of the four-dimensional space–time (gravito-electric contribution) and the dragging of space–time due to central body's rotation (gravito-magnetic contribution).

Montenbruck and Gill (2000) provides the equation for relativistic correction of the acceleration. For a circular orbit around Mars, this acceleration is given by:

$$\mathbf{a}_{\text{relativity}} = -\frac{Gm_{\mathcal{J}}}{r^2}\mathbf{e}_r\left(3\frac{v^2}{c^2}\right) \tag{5}$$

where $\mathbf{e}_r$ is the unit position vector, v is the velocity of the satellite in its circular orbit, $c = 299792458$ m/s is the speed of light, and other symbols have their usual meanings. Tudat uses a more detailed model as described by Luzum and Petit (2012). It is composed of three components, namely Schwarzschild, Lense-Thirring and de Sitter.

3.2.6. Other forces

Other dynamical effects due to Poynting-Robertson drag (e.g. Kuznetsov et al. (2012)), albedo forces, sporadic-weak magnetic field, tides and seasonal variation

in gravity (Smith et al., 2009) are not considered here due to their expected low magnitude and the lack of availability of consistent models.

3.3. Comparison of accelerations

A number of force model elements has been presented previously. However, from the computation-time perspective, it is judicious to use only those elements in the simulations which cause significant accelerations. Fig. 3 presents all accelerations as a function of altitude. This figure will become useful in tuning the propagation settings for the various study cases (Section 4).

Fig. 3 is plotted based on the averaged magnitude of perturbing accelerations in the Martian environment, as presented by Montenbruck and Gill (2000) for Earth. Note that the distances between celestial bodies were averaged, and therefore a straight-line behaviour for third-body forces is seen, instead of a rise to infinity at the Phobos and Deimos altitudes. A slightly different and somewhat more accurate, yet less comprehensive, comparison can be found in the research by Suchantke et al. (2019).

The horizontal line for SRP (plotted using $C_R = 1.3$ and $A/m = 0.01$ m^2/kg) would move up in the plot for a higher value of $C_R A/m$ and conversely fall with a lower value. For the third bodies, apart from the Sun, moons and the planets, contributions from the most perturbing objects, namely dwarf planet Ceres and the asteroids Vesta and Pallas (Mouret et al., 2009) are also included.

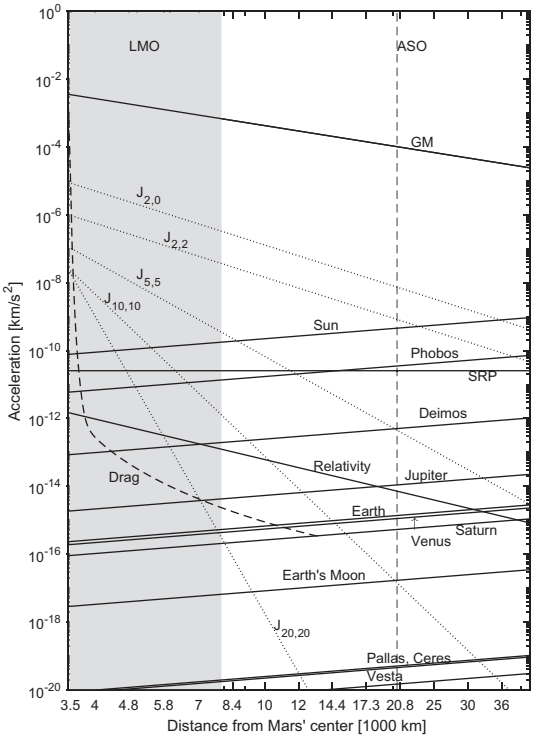

Fig. 3. Average magnitude of accelerations experienced near Mars. $C_R = 1.3$, $C_D = 2.3$ and $A/m = 0.01$ m^2/kg are used. The left boundary of the x-axis can be used as an indication for the surface of Mars.

The issue of selecting the elements of the dynamic model will be further treated in Section 4.

3.4. Equation of motion and parametrization

The following classical equation of motion is used for the simulations in a straightforward manner using Cartesian position and velocity:

$$\ddot{\mathbf{r}} = -\frac{\mu}{r^3}\mathbf{r} + \mathbf{a}_{\text{non-spherical}} + \mathbf{a}_{\text{p}} + \mathbf{a}_{\text{SRP}} + \mathbf{a}_{\text{drag}} + \mathbf{a}_{\text{relativity}} \tag{6}$$

where $\ddot{\mathbf{r}}$ is the acceleration vector of the particle/body under consideration, μ is the gravitational parameter of the central body, $\mathbf{r}$ is the position vector of the particle/-body under consideration and $\mathbf{a}_{\text{non-spherical}}$, $\mathbf{a}_{\text{p}}$ and $\mathbf{a}_{\text{SRP}}$ are the perturbing accelerations due to the non-spherical gravity field of the central body, the perturbing bodies and SRP, respectively.

This simple representation was necessary for the complex symplectic integrator (described in the next subsection) employed in this project. However, Hamiltonian formulations are usually implemented with symplectic integration, and are a good option to explore in the future studies to enhance accuracy/speed.

3.5. Numerical integrator

Multiple past researchers have found that symplectic integration is advantageous for long-term propagation of orbital dynamics (Cintio et al., 2017; Hofsteenge, 2013; Hubaux et al., 2012; Lemaître, 2019; Rosengren et al., 2019). This is because symplectic integrators, unlike non-symplectic ones, conserve energy and angular momentum over long periods of propagations, making them physically consistent. Also, they are less time-consuming compared to their non-symplectic counter-parts of the same order, because they allow larger time-steps, making them highly efficient. Even systems containing non-conservative forces (e.g. SRP, aerodynamic drag) have been found to produce high-quality results using such integrators. The only concern with using symplectic integrators is that they have a fixed step-size with no error-correction possibility, leaving trial-and-error as the only method for choosing the optimal step-size. The decision on step-sizes to be used for our study cases is discussed in the following section.

Symplectic integration is a mathematically complex technique, which requires extensive understanding of symplectic geometry, Lie algebra and Hamiltonian systems. More details on the mathematics involved and its application methods can be found in the works by Fecko (2006), Hairer et al. (2006), Hofsteenge (2013) and Kinoshita and Nakai (1992). The application for long-term astrodynamical propagations of space debris can be found in papers by Breiter and Métris (1998), Breiter et al. (2005), Cintio et al. (2017), Hubaux et al. (2012), Hubaux et al. (2013), Hubaux and Lemaître (2013), Laskar and Robutel (2001), Surovik and Scheeres (2012) and Wytrzyszczak and Breiter (2001).

To establish the soundness of the symplectic integrator implementation in Tudat, three long-term propagation test cases were validated. A 100-year near-Geosynchronous trajectory for a high area-to-mass ratio object showed near-perfect agreement with the results generated by Anselmo and Pardini (2010), while using a step-size of 10% of the orbital period. Also, a low area-to-mass ratio satellite's inclined trajectory in medium Earth orbit was found to be captured perfectly (Fig. 4) when compared to the results from the paper by Rossi (2008), for a 200-year propagation duration with the step-size being 110% of the orbital period. Finally, to validate the propagation settings in the Martian dynamical environment, Deimos' ephemerides (JPL - Chamberlin, 2019) from the year 2050 to 2250 were used. A 100% overlap of Deimos' radial distance from Mars' center was found, with the maximal error attained after 200-year propagation being less than ±10 km (Fig. 5). It is emphasized here that all validations cover a time interval which is comparable if not similar to the interval used in this paper.

3.6. Grid definitions

To provide the (near-) future satellite operators a range of graveyard orbit options to select from, depending on the availability of propellant at EOL, an analysis of long-term stability is performed on a multitude of orbital conditions in the circummartian space. The technique for doing orbital transfers is available in many textbooks on orbital mechanics, but the outcome is of course dependent on the exact problem. Similar evaluations can be found in Colombo et al. (2019) and Schettino et al. (2019) for the Earth case.

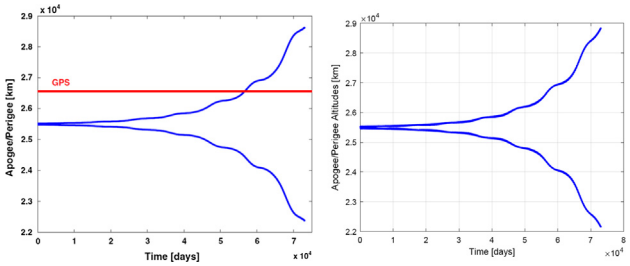

Fig. 4. Validation using apogee and perigee altitude trends over 200 years for the Etalon-2 satellite, with the left plot from Rossi (2008) and the right plot generated numerically by symplectic propagation in th.e current study.

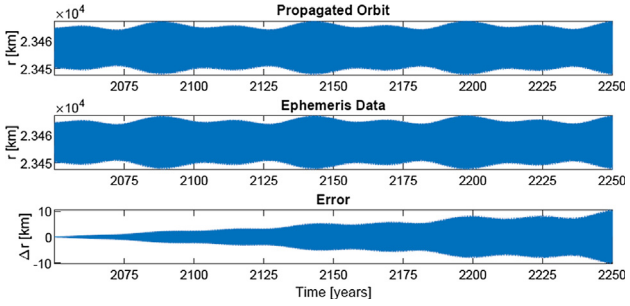

Fig. 5. Validation of symplectic integration in Martian environment using Deimos' position from Mars' center.

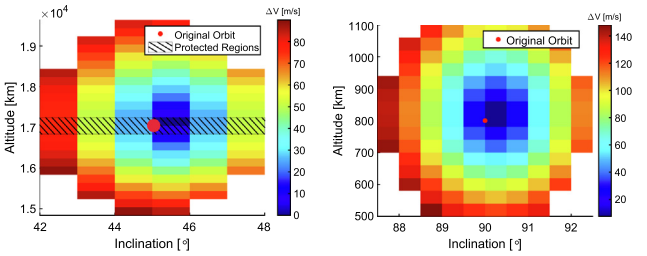

(a) ASO (17038 km altitude) with 45° inclination.

(b) LMO with 800 km altitude and 90° inclination.

Fig. 6. ΔV map for transfer from operational to graveyard orbits.

Fig. 6a shows the grid points for the ASO 45 case in altitude-inclination space, with color representing the ΔV required for the transfer from a 45° inclined ASO to the grid points. The ΔV values were calculated using a two-burn Hohmann transfer assumption. Each grid point has the dimensions of 200 km by 1°, and the grid is restricted to a maximum ΔV of 90 m/s. Similarly, Fig. 6b shows the grid points for the LMO 90 case. The grid-point size here is 40 km by 0.5°. The grid is restricted to a maximal ΔV value of 150 m/s, which is expected to be the maximum available value at EOL (Subsection 2.2), for this tightly bound low-altitude region. The study grids and results for the ASO 0 and LMO 0 cases are identical to the left halves of their respective inclined counterparts and are therefore not shown here. Such a grid analysis would help satellite operators make appropriate trade-offs among available ΔV, stability, maneuver complexity, regulations, economic viability, collision avoidance, etc.

4. Tuning propagation settings

Thousands of 200-year propagations are to be carried out over the grids discussed previously, for different values for the initial Ω and A/m. Thus, it is imperative to determine the optimal propagation settings, namely the integrator step-size and force model combinations, such that the accuracy of the solutions is as high as possible while the computation times are within practical limits.

The results of extremely accurate baseline simulations, which are assumed to be 100% identical to 'reality', are compared to simulations executed with various types of propagation settings for various types of study conditions. The accuracy of the propagation settings is determined by the divergence of five crucial parameters compared to the baseline runs. These include the maximum eccentricity achieved during the 200-year simulation ($e_{\max}$), computation time, the maximum and minimum distances from Mars' center reached during the propagation ($r_{\max}$ and $r_{\min}$) and the maximum inclination change from the nominal value ($\Delta i_{\max}$).

4.1. ASO regime

To tune the propagation settings for various types of satellite/orbit characteristics in the ASO regime, eight cases are identified. These are composed of two altitude, two inclination and two C_RA/m values ($2 \times 2 \times 2$). Altitude values include ASO altitude $\pm(200 + 10^3 * C_RA/m)$ km. Inclinations used are the most prominent 0° and 45°. Finally, the two extreme C_RA/m values of 0.013 m^2/kg and 1.9 m^2/kg are chosen for this tuning analysis.

A baseline run for each of the eight cases was performed with very high accuracy settings. Namely, a force model including all accelerations whose average magnitude at ASO altitude is larger than 10^{-18} km/s^2 (based on Fig. 3 along with the areopotential up to degree and order 15) and an integrator step-size of 0.1 Julian days (JD). These results are deemed to be 'true-to-reality', based on the accuracy of the integrator validation results (Subsection 3.5) and the settings used by Anselmo and Pardini (2010) and Rossi (2008).

Nine types of propagation settings are analysed (3 *force models* x 3 *integrator step-sizes*). These include 'low', 'medium' and 'high' environment accuracy settings and include all accelerations whose average magnitude at ASO altitude is larger than $10^{-12}, 10^{-15}$ and 10^{-18} km/s^2, respectively (again, based on Fig. 3). The integrator step-size options include 0.5, 1.0 and 2.0 JD.

Table 1 presents the results of the tuning analysis for the eight cases for each of the nine types of propagation settings. The ticks represent the settings which are deemed acceptable based on the decision parameters discussed above, such that the r_{max} and r_{min} divergence from the baseline values is less than about 10 km over 200 years. Only the 'high' environment accuracy setting with a step size of 0.5 JD is seen to be acceptable for all cases. However, use of this would lead to anywhere from double to sevenfold as much computation time as others, resulting in CPU times of days, if not weeks. Thus, the next-best option of 'low' environment accuracy with a step size of 0.5 JD is used for ASO regime simulations. This includes the areopotential up to degree and order 4, SRP and third-body perturbations due to the Sun, Phobos and Deimos. Note that with this setting, only the inclined high A/m case (Case 6) would produce a large error in r_{max} and r_{min} of about 25 km, which is deemed acceptable, so that consistent fidelity settings can be selected for all graveyard orbit simulations in the ASO regime.

4.2. LMO regime

12 cases ($3 \times 2 \times 2$) are identified for various satellite/orbit characteristics in the LMO regime. These include: three altitudes of 200, 800 and 1400 km; 0° and 90° inclinations; and two A/m values of 0.01 and 0.1 m^2/kg (with $C_R = 1.3$ and $C_D = 2.3$).

Table 1
Acceptable propagation settings for cases in ASO regime (bold-green tick indicates the optimum for each case).

Case \ Propagation settings	**Low, 0.5 JD**	**Low, 1.0 JD**	**Low, 2.0 JD**	**Med, 0.5 JD**	**Med, 1.0 JD**	**Med, 2.0 JD**	**High, 0.5 JD**	**High, 1.0 JD**	**High, 2.0 JD**
1 $C_RA/m = 0.013$ m^2/kg, ASO ↑, $i = 0^\circ$	✓	✓	**✓**	✓	✓	✓	✓	✓	✓
2 $C_RA/m = 0.013$ m^2/kg, ASO ↑, $i = 45^\circ$	✓	**✓**		✓	✓		✓	✓	
3 $C_RA/m = 0.013$ m^2/kg, ASO ↓, $i = 0^\circ$	✓	✓	**✓**	✓	✓	✓	✓	✓	✓
4 $C_RA/m = 0.013$ m^2/kg, ASO ↓, $i = 45^\circ$	✓	**✓**		✓	✓		✓	✓	
5 $C_RA/m = 1.9$ m^2/kg, ASO ↑, $i = 0^\circ$	**✓**						✓		
6 $C_RA/m = 1.9$ m^2/kg, ASO ↑, $i = 45^\circ$			**✓**	✓	✓		✓	✓	
7 $C_RA/m = 1.9$ m^2/kg, ASO ↓, $i = 0^\circ$	✓					✓			✓
8 $C_RA/m = 1.9$ m^2/kg, ASO ↓, $i = 45^\circ$	✓	**✓**		✓	✓		✓	✓	

The force model for the very accurate baseline simulations included all accelerations whose average magnitude in the LMO region is larger than 10^{-18} km/s^2 (based on Fig. 3 along with an areopotential up to degree and order 40). The step-size used for the integrator is 0.005 JD, which translates to 15 computation steps per orbit at 200 km altitude. Since no prior data on long-term propagation in the highly dynamic environment of the LMO region exists (at the time of writing this paper), this 15-steps-per-orbit simulation was validated against a 150-steps-per-orbit one, because as per Vallado and McClain (2001) 100 integration steps per orbital revolution are satisfactory for standard applications. The results were found to be in 100% agreement for the purpose of this paper, assuring that a 0.005 JD step-size and the selected force model provide an accurate representation of 'reality'.

Six types of propagation settings options are examined (2 *force models* x 3 *integrator step-sizes*). These include: a 'low'-fidelity setting with the areopotential up to degree and order 10 and aerodynamic drag; and a 'high'-accuracy setting with areopotential up to degree and order 30, aerodynamic drag, SRP and third-body perturbations from the Sun and Phobos. The integrator step-size options are 0.01, 0.05 and 1.0 JD.

Table 2 presents the results of the tuning analysis in the LMO regime. The 'low'-fidelity setting contains all the optima (determined mainly by computation times), while the step sizes at which they occur differ for different cases. Thus, after a short analysis, it can be concluded that the following step-sizes, along with 'low'-accuracy settings, are optimal for various altitude ranges: 0.01 JD for 200 to 400 km, 0.05 JD for 400 to 1200 km and 0.1 JD for 1200 to 1400 km.

5. Stability results and sensitivity

This section presents the stability results and their sensitivity for the four study cases. This involves employing the symplectic integration technique, using the optimal propagation settings, on the grid of circummartian orbital conditions to come up with plots that provide the maximal deviation in radial distance w.r.t. the nominal value ($\pm\Delta r_{max}$). Furthermore, four initial Ω values of $0°, 90°, 180°$ and $270°$ were used to understand the potential impact of the initial condition on stability. Also, multiple A/m values were investigated. Only the most relevant results are presented here.

5.1. Areostationary orbits

For objects with low A/m values in candidate AEO graveyard orbits, the maximal deviation in r_{max} is less than 30 km in both the inward and the outward direction for almost all altitude-inclination combinations analysed (Fig. 7). This maximal deviation increases to 140 km for high A/m objects (Fig. 8). Spending only about 10 m/s ΔV to transfer an AEO satellite to 400 km below the nominal orbital altitude (Fig. 6a) would ensure a $\pm$25 and $\pm$125 km stability for C_RA/m values of 0.013 and 0.13 m^2/kg, respectively, for at least 200 years. For the configuration with $C_RA/m = 1.9$ m^2/kg, the best option to (barely) avoid crossing the protected zone is to transfer this light satellite to 1400 km below the nominal ASO altitude by expending 50 m/s of ΔV and is thus not discussed further.

In general, lower-than-nominal altitudes are found to be more stable compared to the higher ones. Also, the radial deviations in inward direction ($-\Delta r_{max}$) are found to be slightly larger than those in the outward direction ($+\Delta r_{max}$) and thus plots for only the former are presented in this paper. Also, the plots deem any inclination change, to achieve a stable orbit, unnecessary. In fact, they suggest that any transfer errors leading to variations in the nominal inclination have negligible effect on the stability (except from the slight variations with inclination seen in the $\Omega = 90°$ plot in Fig. 7). Stability is found to have a weak correlation with the initial orientation of the orbital plane or Ω for AEO satellites.

To take into account the uncertainties and establish the robustness of a chosen graveyard orbit solution, a sensitivity analysis is performed. The effect of orbit insertion errors can partially be understood by the altitude-inclination plots of stability for various Ω values (such as Fig. 7). How-

Table 2
Acceptable propagation settings for cases in LMO regime (bold-green tick indicates the optimum for each case).

	Case \ Propagation settings	**Low, 0.01 JD**	**Low, 0.05 JD**	**Low, 0.1 JD**	**High, 0.01 JD**	**High, 0.05 JD**	**High, 0.1 JD**
1	$C_RA/m = 0.013$ m^2/kg, 200 km, $i = 0°$	✓			✓		
2	$C_RA/m = 0.013$ m^2/kg, 200 km, $i = 90°$	✓	✓		✓		
3	$C_RA/m = 0.013$ m^2/kg, 800 km, $i = 0°$	✓	✓	✓	✓	✓	✓
4	$C_RA/m = 0.013$ m^2/kg, 800 km, $i = 90°$	✓	✓		✓	✓	
5	$C_RA/m = 0.013$ m^2/kg, 1400 km, $i = 0°$	✓	✓	✓	✓	✓	✓
6	$C_RA/m = 0.013$ m^2/kg, 1400 km, $i = 90°$	✓	✓	✓	✓	✓	✓
7	$C_RA/m = 0.13$ m^2/kg, 200 km, $i = 0°$	✓	✓		✓	✓	
8	$C_RA/m = 0.13$ m^2/kg, 200 km, $i = 90°$	✓			✓		
9	$C_RA/m = 0.13$ m^2/kg, 800 km, $i = 0°$	✓	✓		✓	✓	
10	$C_RA/m = 0.13$ m^2/kg, 800 km, $i = 90°$	✓	✓		✓		
11	$C_RA/m = 0.13$ m^2/kg, 1400 km, $i = 0°$	✓	✓	✓	✓	✓	✓
12	$C_RA/m = 0.13$ m^2/kg, 1400 km, $i = 90°$	✓	✓	✓	✓	✓	✓

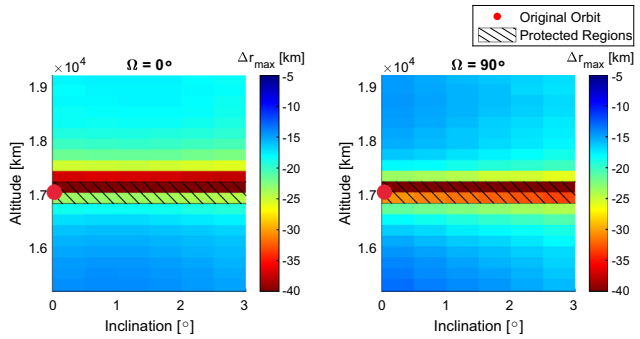

Fig. 7. Maximal altitude deviation for ASO graveyard orbits with 0° inclination and $C_RA/m = 0.013$ m^2/kg.

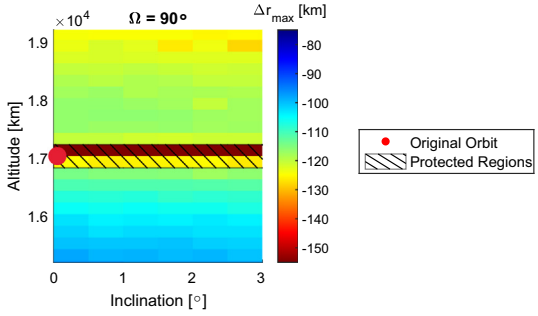

Fig. 8. Maximal altitude deviation for ASO graveyard orbits with 0° inclination and $C_RA/m = 0.13$ m^2/kg.

ever, the tolerance allowed in the eccentricity error is also highly crucial to consider when selecting a graveyard orbit. Apart from the orbit insertion errors, the possibility of uncontrolled satellite tumbling after EOL could significantly modify the A/m ratio and thus perturb the nominal graveyard orbit.

Fig. 9a shows the cumulative effects of an error in the initial eccentricity and tumbling on the AEO graveyard orbit's altitude. Twice and half of the nominal A/m values are used as bounds for tumbling uncertainty (shaded regions), based on research by Früh and Schildknecht (2012) and considering the cuboidal-shaped *MRO*'s dimensions (JPL, 2006a) as representative for Mars spacecraft; tumbling is assumed to be completely random, both in direction and frequency. The red line in the plot marks

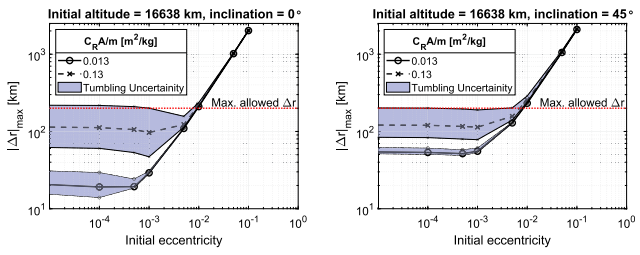

(a) 0° inclination. (b) 45° inclination.

Fig. 9. Sensitivity in $|\Delta r|_{max}$ for uncertain e and A/m for ASO graveyard orbits.

the upper limit of the maximum allowed altitude variation so that the protected regions around ASO are not crossed. Thus, the maximal uncertainty allowed in the initial eccentricity is 0.01 for both C_RA/m cases. The flat nature of the curves until a certain eccentricity and a subsequent sharp(-merged) rise is attributed to SRP's nature. SRP adds only small perturbations to r, and when the initial orbit itself is sufficiently elliptical, SRP's minuscule perturbations (and thus the impact of A/m) become insignificant.

5.2. Areosynchronous orbits - 45° inclination

For 45° inclined ASO graveyard orbits, the radial deviation from the nominal altitude is always less than 90 and 170 km for heavy and light satellite configurations, respectively (Figs. 10 and 11). It is noteworthy that graveyard orbits near inclined ASO are less stable compared to their equatorial counterparts. Another readily observed peculiarity here is that the initial Ω and i values have strong effects on stability, unlike in the AEO case. In Fig. 10 the i-Ω combination significantly affects stability, whereas in Fig. 11 inclination, for each Ω case, in itself is not affecting the stability significantly, but the different Ω values do affect it at specific inclination-altitude combinations.

Although the safest graveyard orbit is dependent on initial Ω and i, in general it can be said that raising or lowering the altitude by 400 km is a safe choice for a graveyard orbit, irrespective of the initial value of Ω. This would consume around 10 m/s of ΔV (as per Fig. 6a) and would lead to orbits that deviate from the original orbits (to a maximum of) around ±80 and ±150 km over a 200-year period.

Fig. 9b shows that the maximum uncertainty an operator can afford (to avoid entering the ASO protected zone)

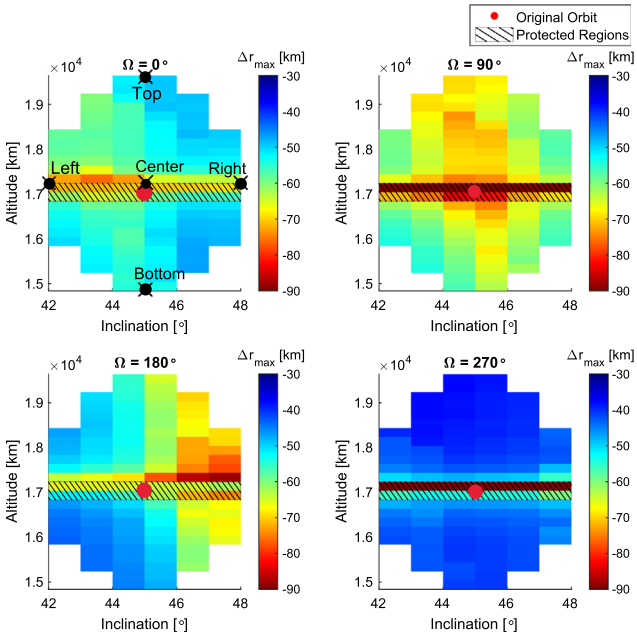

Fig. 10. Maximal altitude deviation for ASO graveyard orbits with 45° inclination and $C_RA/m = 0.013$ m^2/kg.

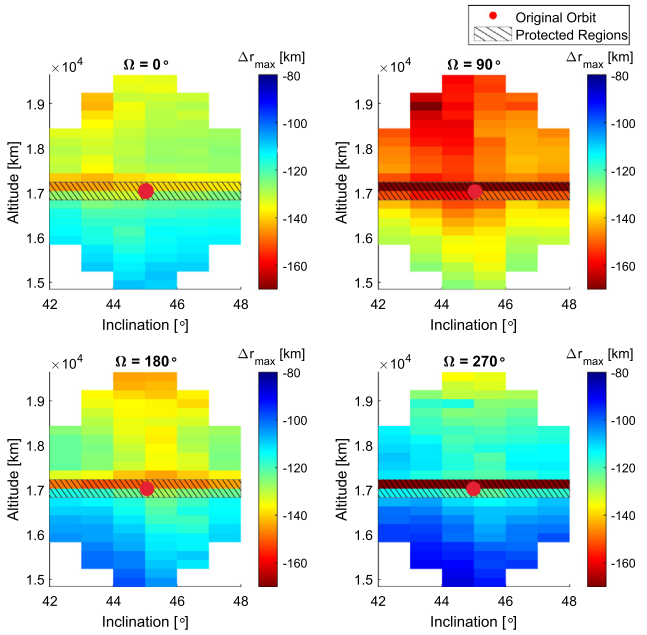

Fig. 11. Maximal altitude deviation for ASO graveyard orbits with 45° inclination and $C_RA/m = 0.13$ m^2/kg.

in initial eccentricity is 0.008 for a satellite with a C_RA/m of 0.013 m^2/kg and 0.005 for a satellite with a C_RA/m of 0.13 m^2/kg. Tumbling is completely acceptable. Note that the smaller width of the tumbling bands compared to the AEO uncertainty, shows that inclined orbits are less susceptible to such a situation.

5.3. Low Mars orbits - 0° inclination

The radial deviation for most of the points in the plots (Figs. 12a and 12b) are below 25 and 60 km for low and high A/m valued objects, respectively, due to the difference in aerodynamic drag experienced in the two configurations. This implies that orbits in the LMO region are fairly stable even for 200 years, unlike Earth's low altitude orbits. Only the cases with an initial $\Omega = 0°$ are presented here because the results are almost identical for other values of Ω. Note that some altitudes show special instability. Areopotential resonance at these altitudes is the probable cause for this. Also the lowest altitude of 500 km is significantly less stable compared to others, which is expected due to a denser atmosphere.

The deviations for radially outward direction ($+\Delta r_{\max}$) are found to be much smaller compared to the inward direction ($-\Delta r_{\max}$). Thus, the optimal option to avoid a collision with an operational satellite at 800 km (the original situation) would be to transfer to a lower-than-nominal altitude. So, for the $C_DA/m = 0.023$ m^2/kg case, lowering the satellite's altitude by 60 km by spending around 20 m/s ΔV (Fig. 6b), a stable graveyard orbit can be achieved. For the $C_DA/m = 0.23$ m^2/kg case, on the other hand, a change in altitude of ±100 km seems relevant which would require around 30 m/s ΔV.

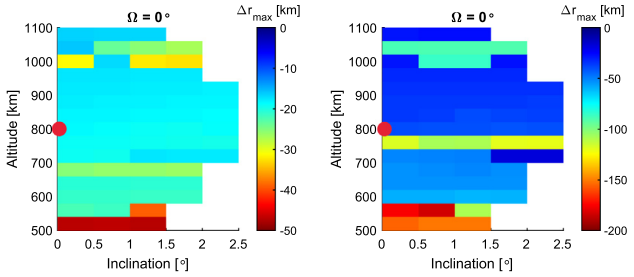

(a) $C_DA/m = 0.023$ m^2/kg. (b) $C_DA/m = 0.23$ m^2/kg.

Fig. 12. Maximal altitude deviation for LMO graveyard orbits with initial altitude 800 km and inclination 0° (red dot indicates original orbit geometry).

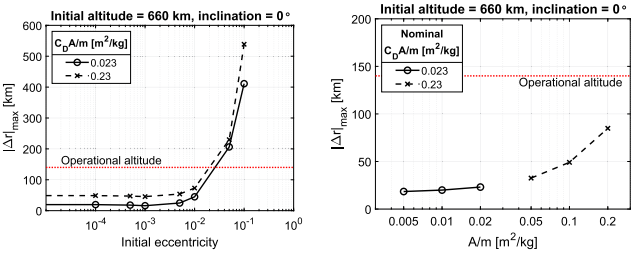

(a) Uncertainty in e. (b) Uncertainty in A/m.

Fig. 13. Sensitivity in $|\Delta r|_{\max}$ for uncertain e and A/m for LMO graveyard orbits with 0° inclination.

Uncertainties in eccentricity and tumbling are treated separately in Fig. 13. It can be observed in Fig. 13a that the maximal affordable uncertainty (i.e. to avoid crossing the operational orbit) in initial eccentricity is 0.025 for the $C_DA/m = 0.023$ m^2/kg case and 0.02 for the case with $C_DA/m = 0.23$ m^2/kg. A sharp rise in $|\Delta r|_{\max}$ is seen in the right end of the curve because as the eccentricity becomes sufficiently large, the denser atmosphere's aerodynamic drag becomes significant and takes over the dynamics. Fig. 13b shows the tumbling uncertainty's effects. The middle marker on each of the two lines represents the original (starting) condition and the extreme points represent the possible range of A/m due to tumbling. It shows that all tumbling configurations keep at least more than 50 km away from the operational altitude for this 660 km 0° inclination orbit, thus assuring safety after EOL. Both trends are regular and can thus be safely interpolated for further analysis.

5.4. Low Mars orbits - 90° inclination

For disposal of satellites in polar LMO or Sun-synchronous orbits around Mars, Fig. 14 presents the long-term stability results. The $\Delta r_{\max}$ values are found to be very irregular in the inclination-altitude space, and much less stable compared to non-inclined orbits. Different initial orientations of the orbital plane or values of Ω show different effects on the 'colourful' unstable regions, but are inconsequent for long-term stability in the relatively stable

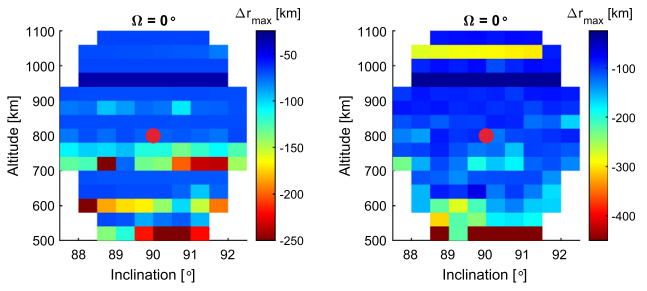

(a) $C_DA/m = 0.023$ m^2/kg. (b) $C_DA/m = 0.23$ m^2/kg.

Fig. 14. Maximal altitude deviation for LMO graveyard orbits with initial altitude 800 km and inclination 90° (red dot indicates original orbit geometry).

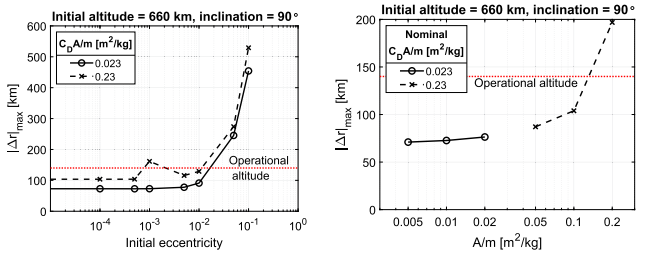

(a) Uncertainty in e. (b) Uncertainty in A/m.

Fig. 15. Sensitivity in $|\Delta r|_{\max}$ for uncertain e and A/m for LMO graveyard orbits with 90° inclination.

regions. However, even for the stable regions, these polar orbits are much less stable compared to equatorial orbits (examined in the previous subsection) for the same C_DA/m value. The lower orbits show a significant variation with only a small inclination change at the same altitude.

The options that are most feasible and stable, closest to the nominal orbit, are at 660 and 900 km. These altitudes are relatively more stable and unaffected by i and Ω values. This would require spending about 60 or 30 m/s of ΔV (Fig. 6b), respectively. However, it should be realized that transferring to 900 km would lead to a graveyard orbit that would miss the operational orbit by only about 40 km in its lifetime.

The highly stable band seen at 940 km altitude points out the drawback of using a computation step-size which is half the orbital period for an inclined orbit. The dynamical effects are calculated in the simulation at the same latitude location repeatedly for this polar orbit. Thus, this does not indicate any speciality in the physics of the problem but a numerical discrepancy which can be resolved by using a smaller/larger step-size.

Fig. 15a shows that the maximal uncertainty allowed in initial eccentricity is 0.018 for the $C_DA/m = 0.023$ m^2/kg case and 0.01 for the $C_DA/m = 0.23$ m^2/kg case. These values are almost half the allowed values for equatorial LMO's, reiterating that not only inclined orbits are less stable, but also that they are more susceptible to uncertainties, which is unlike the ASO case (Fig. 9). Furthermore, Fig. 15b shows that the satellite with $C_DA/m = 0.023$ m^2/kg is safely separated from the operational altitude for all tumbling configurations. However, for the satellite with $C_DA/m = 0.23$ m^2/kg, the $|\Delta r|_{\max}$ value rises sharply with A/m and crosses the operational orbit with only about 20% increase from the nominal A/m. Therefore, to avoid interaction with anything at the operational altitude, the maximal limit value of A/m for a satellite with an average $C_D = 2.3$ is about 0.12 m^2/kg for a 660 km near-polar orbit.

6. Preliminary interpretation

It is imperative to understand what physical factors are causing the variations in the results shown in the previous section as a function of altitude, inclination, right ascension of ascending node, etc. This section analyses, explores and attempts to understand those reasons.

Note that this section should be treated only as an introduction to a more comprehensive interpretation, which should be thoroughly carried out in future research. The results derived in the previous section are addressed here from a variety of perspectives in a preliminary manner only, attempting to draw on the theories developed for terrestrial orbits research. This section by no means attempts to give a comprehensive theoretical understanding of the results, but only attempts to 'practically' assess the results.

6.1. Radius vs. time

Radial distance as function of time is analysed for the five points marked *left*, *center*, *right*, *bottom* and *top* in Fig. 10 for the ASO 45 case. Figs. 16 and 17 are used to examine the effects including/excluding Sun (solar gravity and SRP) in the force model, for the initial Ω values of 180° and 270°, respectively.

SRP is found to add only small perturbations. This can be observed in the full-model curves in Figs. 16 and 17 as high-frequency low-amplitude aberrations of less than about 10 km from smoothness. Two distinct types of effects of solar gravity are broadly observed depending on the different starting conditions (i.e. Ω and altitude combinations). A: It flattens the 'beat'-shaped wave observed in r over time. B: It widens the beat amplitudes by increasing both the minimal and maximal amplitudes. Fig. 18 gives the locations where these effects are found. The grid of white spaces represents the five study points mentioned above (in their logical locations). Solar gravity is also found to affect inclination trends differently depending on the Ω-altitude combinations.

Also, it is speculated that the stability decreases with altitude in general, because of SRP: at higher altitudes the relative magnitude of the SRP force is higher compared to Mars' gravity pull. Another reason is that when the orbital radius increases, a larger percentage of the satellite's orbit is exposed to solar radiation. This argument is also

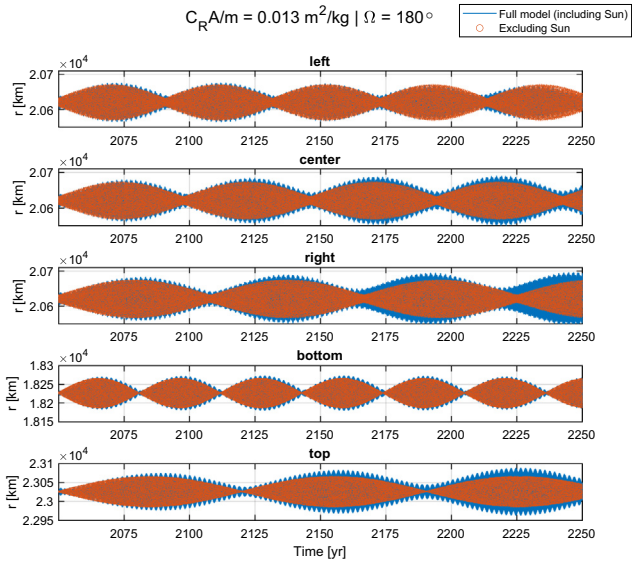

Fig. 16. Time history of radius for various initial graveyard orbit geometries in the ASO 45 regime ($\Omega = 180°$).

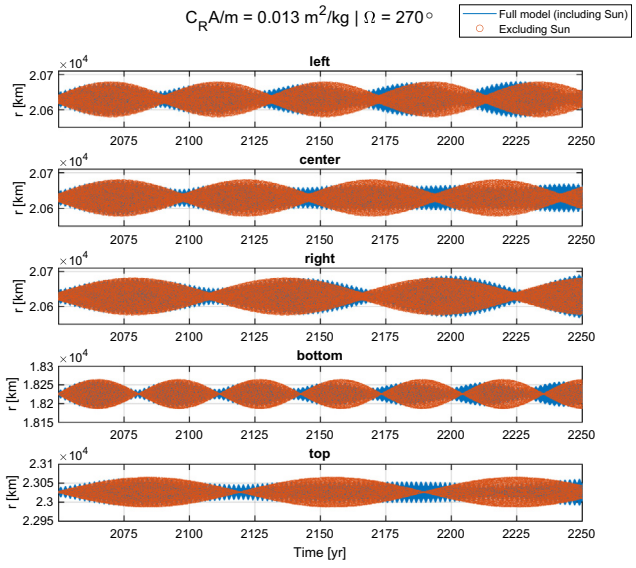

Fig. 17. Time history of radius for various initial graveyard orbit geometries in the ASO 45 regime ($\Omega = 270°$).

validated when the Δr_{max} plots for $C_R A/m$ values of 0.013 and 0.13 m^2/kg are compared (Figs. 10 and 11). It is observed that altitude plays a more prominent role in the latter, which is inherently more prone to SRP perturbations.

Note that the analysis presented in this section is very preliminary and deserves meticulous investigation in future studies. Major in-depth research on the effects of SRP and solar gravity for long-term orbital propagations in non-Martian context has been carried out by researchers such as Alessi et al. (2017), Davis et al. (2008), Harwood and Swinerd (1995), Kubo-oka (1999), Luo and Wang (2019), Wang et al. (2020), Zhao et al. (2017), etc., which needs to be taken into account for further analysis.

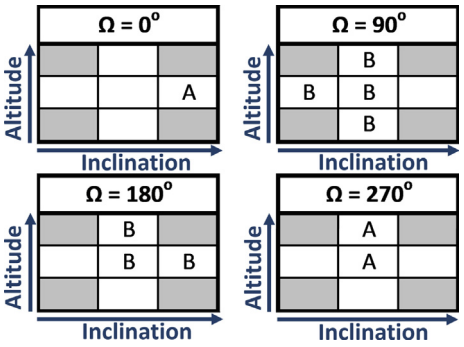

Fig. 18. Effect of solar gravity on r.

6.2. Force angles

To further analyse the physics (related to solar gravity's effect) behind the dynamics, two angles, namely θ_H and θ_{Sat} (Fig. 19) are studied over the full duration of the simulation. θ_H is defined as the angle between the vector from Mars' center to Sun's center and orbital angular momentum vector. θ_{Sat} is defined as the angle between the vector from Mars' center to Sun's center and satellite's instantaneous position vector.

θ_H helps to determine the orientation of the orbital plane with respect to the Sun direction. It is suspected that different initial starting orientations (i.e. altitude-inclination combinations) lead to a different behaviour of this angle over the propagation period. Thus, frequency-histograms of this angle are plotted and the plot corresponding to the initial $\Omega = 0°$ is shown in Fig. 20 for all five chosen analysis points.

When the Sun makes a near-90° angle with the angular momentum vector, the force it exerts on the satellite is in the orbital plane. Conversely, when the angle is near 0° or 180°, the force acts in the perpendicular direction. Fig. 20 clearly shows how the *left*, *center* and *right* positions show variations in the amount of time spent in the 65°-115° range. This implies that the time spent in the near-90° regime is a function of initial inclination of the satellite (because the *left* (blue) line corresponding to 42° initial inclination is above the *top* (green), *center* (orange) and *bottom* (purple) lines, which all correspond to 45° initial inclination. These in turn are all above the *right* (yel-

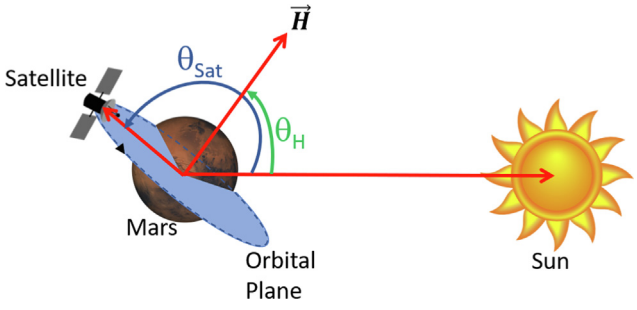

Fig. 19. Angles with Sun direction vector.

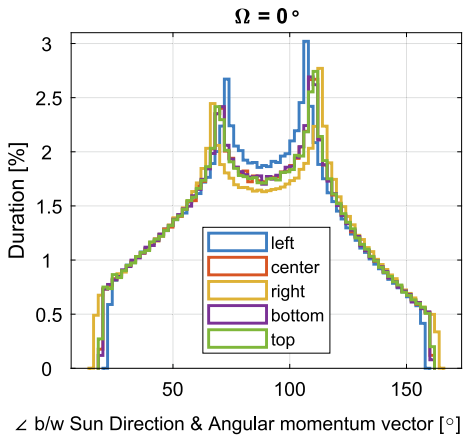

Fig. 20. Frequency histograms for θ_H.

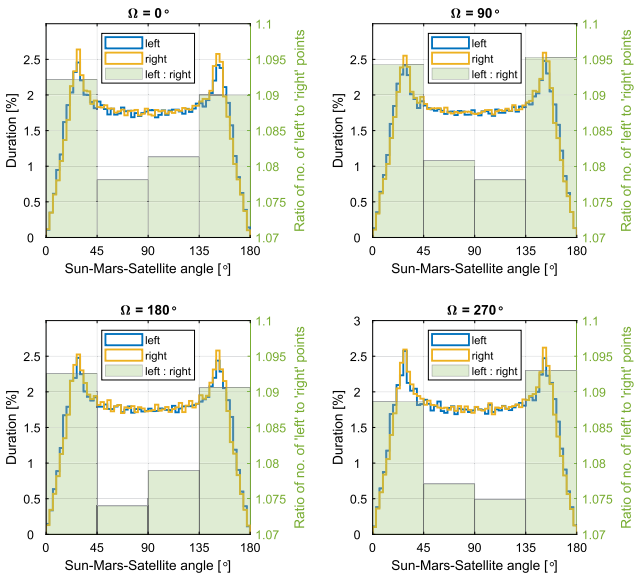

Fig. 21. Frequency histograms for θ_{Sat}.

low) line corresponding to 48° initial inclination.) A similar trend is seen in all four Ω cases. Examining the plot while comparing it with the first subplot in Fig. 10, explains the reasons for the stability to increase from *left* to *right*. This is because *left* (blue) experiences more in-plane forces, thus affecting r_{max} more strongly, compared to the *top* (green), *center* (orange) and *bottom* (purple) geometries. Similarly, these three experience more in-plane forces compared to the *right* (yellow) case. Thus stability increases towards the *right* end of the grid in Fig. 10.

Though a thorough plot, Fig. 20 alone does not provide us all information. Determining the frequency of the force experienced in or out of the orbital plane does not inform us on the direction in which the force is actually acting on the satellite. Even in a hypothetical scenario, if the force is in 100% alignment with the orbital plane for the whole propagation duration (i.e. 90° with 100% duration in Fig. 20), the force direction could vary from being anywhere in the radial to along-track directions. The frequency of this direction would further impact stability very differently. Thus, θ_{Sat}, which gives the angle between the line joining Mars' center to the Sun's position and the line joining Mars' center to the satellite position (Fig. 19), is also analysed.

Fig. 21 shows θ_{Sat} frequency-histograms for the *left* (blue) and *right* (yellow) cases. It also shows the ratio of frequencies of *left* to *right* cases for angle ranges of 0° to 45°, 45° to 90°, and so on. Note that to analyse near-in-plane forces, this figure contains only those points in orbit whose θ_H ranges from 65° to 115°. Therefore, a (near) 180° angle in this figure implies that both the solar gravity force and planetary gravitation are acting in the same i.e. negative radial direction. Conversely, (near) 0° means that the solar gravity force and planetary gravitation are acting in opposite directions, though still along the radial direction.

The middle two ratio-bars (green) in the first ($\Omega = 0°$) and the third ($\Omega = 180°$) plots show that (when the orbital plane is parallel to the Sun direction), *left* (blue) experiences more force in along-track direction in the first than in the third case. Therefore, *left* (blue) is more stable in the third subplot compared to the first in Fig. 10. This is expected due to a stronger along-track force in the first one causing a greater eccentricity change, which is less in the third subplot. Similar explanations can be given for the other trends.

6.3. Note on validity of the interpretations

It should be noted that to limit the scope of the study, several relevant concepts have merely been introduced here, without delving deep into the theoretical details, on which a more comprehensive research can be built. Therefore, the considerations drawn here might be heuristic. For example, the theory behind SRP needs to be studied in detail to arrive at more detailed interpretation of the results produced in the previous sections. In addition, the reader is recommended to refer to the following works to explore the topic of resonance: Hughes (1980), Ineichen et al. (2003), Kaula (1966), Rosengren et al. (2019), Rossi (2008), Wakker (2015), etc. The results obtained in this paper deserve a serious interpretation, on the basis of a precise theoretical development, to develop a better understanding of the reasons of the detected behaviours in future studies.

7. Conclusions

The symplectic integration technique is found to give accurate results for long-term propagations in a Martian environment, with an error of ±10 km over a 200-year period. Only a few computation steps (less than five) per orbital revolution are found to be sufficient.

For propagation of Areosynchronous orbits, the use of the following force model elements is found to be an optimum choice: areopotential up to degree and order four, solar radiation pressure, and the third bodies Sun, Deimos and Phobos (as point masses). For propagation of low

Mars orbit satellites, the optimal force model settings include areopotential up to degree and order 10 along with aerodynamic drag.

Spending about 10 m/s ΔV to transfer an ASO satellite to about 400 km below nominal altitude, is found to be sufficient to achieve long-term stability such that the satellite would not interfere with the protected zones, irrespective of the initial orientation of the orbital plane (Ω). Such a transfer would ensure variations in debris object's altitude from graveyard altitude of ± 25 and ± 120 km near-Areostationary orbits with a $C_R A/m$ of 0.013 and 0.13 m^2/kg, respectively. For 45° inclined ASO, this would ensure variations of ± 80 and ± 150 km from the nominal graveyard altitude for $C_R A/m$ values of 0.013 and 0.13 m^2/kg, respectively.

However, the eccentricity uncertainty during insertion into the graveyard orbit should be less than 0.01 for AEO's to avoid interactions with the protected zones. Similarly, for inclined ASO it should be less than 0.008 and 0.005 for satellites with effective $C_R A/m$ values of 0.013 and 0.13 m^2/kg, respectively. It is found that the uncertainties generated due to tumbling are acceptable and the debris object would barely touch the protected zone in case the effective A/m doubled due to attitude variations.

A spacecraft with a ballistic coefficient $C_R A/m = 1.9$ m^2/kg studied for the areosynchronous regime is found to produce highly unstable graveyard orbits. Such a light satellite would necessitate a transfer to 1400 km below the nominal one, which would cost 50 m/s in ΔV. Thus, a satellite with such a configuration should be avoided around Mars, from a stability perspective.

In general, lower-than-nominal orbits are found to be more stable, due to the ratio of solar radiation pressure to areopotential forces experienced by the satellites. SRP adds only small perturbations in the radial direction for low values of $C_R A/m$. Solar gravity, on the other hand, plays a significant role in perturbing orbits with different initial orientations uniquely. Thus, although the above-mentioned transfers are enough for safe disposal, initial conditions are consequential in determining the degree of long-term stability.

Graveyard orbits near equatorial Low Mars orbits are found to be quite stable both below and above the nominal altitude of 800 km. Spending about 20–30 m/s ΔV for transferring derelict object to 60–100 km off-nominal altitude is found to be sufficient for operational altitude avoidance over a 200-year period for $C_D A/m$ values ranging between 0.023 and 0.23 m^2/kg.

Near-polar LMO graveyard orbits show more dynamic variation with altitude and inclination, as compared to other cases. Also, they are significantly less stable compared to their equatorial counterparts. In general, even for ASO, inclined orbits are less stable compared to non-inclined ones. The near-polar LMO would require at least 30–60 m/s to transfer to more than 100 km beyond nominal, so as to (barely) avoid crossing nominal orbits.

As per sensitivity of LMO graveyard orbits, a wide range of differences are found in the allowed uncertainties. An initial eccentricity deviation of less than about 0.01 would be sufficient for stability in most cases. For tumbling, only the polar LMO with a high $C_D A/m$ value of 0.23 m^2/kg should not tumble beyond 1.2 times its nominal value. Others can bear half to double their nominal A/m values.

In conclusion, using graveyard orbits is a feasible and cheap option as Martian satellite's end-of-life strategy, for the whole circummartian space. The plots provided here can help operators to select graveyard orbits of choice depending on the expected availability of ΔV at EOL. The results could also be used to decide the reserve ΔV to carry for EOL, during the design phase of the missions. Finally, this could also be used by regulators and law-makers to define protected and safe disposal zones, while also issuing guidelines and imposing regulations on future satellites around Mars.

Declaration of Competing Interest

The authors declare that they have no known competing financial interests or personal relationships that could have appeared to influence the work reported in this paper.

References

Alessi, E.M., Deleflie, F., Rosengren, A.J., Rossi, A., Valsecchi, G.B., Daquin, J., Merz, K., 2016. A numerical investigation on the eccentricity growth of GNSS disposal orbits. Celestial Mech. Dyn. Astron. 125 (1), 71–90. https://doi.org/10.1007/s10569-016-9673-4.

Alessi, E.M., Schettino, G., Rossi, A., Valsecchi, G.B., 2017. Solar radiation pressure resonances in low Earth orbits. Mon. Not. R. Astron. Soc. 473 (2), 2407–2414. https://doi.org/10.1093/mnras/stx2507.

Alessi, E.M., Schettino, G., Rossi, A., Valsecchi, G.B., 2018. Natural highways for end-of-life solutions in the LEO region. Celestial Mech. Dyn. Astron. 130 (5), 34. https://doi.org/10.1007/s10569-018-9822-z.

Allan, R.R., Cook, G.E., Lighthill, M.J., 1964. The long-period motion of the plane of a distant circular orbit. Proc. Roy. Soc. London. Series A. Mathe. Phys. Sci. 280 (1380), 97–109. https://doi.org/10.1098/rspa.1964.0133.

Anselmo, L., Pardini, C., 2010. Long-term dynamical evolution of high area-to-mass ratio debris released into high Earth orbits. Acta Astronaut. 67 (1), 204–216. https://doi.org/10.1016/j.actaastro.2009.10.017.

Bell, D.J., Cesarone, R., Ely, T., Edwards, C., Townes, S., 2000. Mars network: a Mars orbiting communications and navigation satellite constellation. In: 2000 IEEE Aerospace Conference proceedings (Cat. No.00TH8484), vol. 7. pp. 75–88. https://doi.org/10.1109/AERO.2000.879277.

Breiter, S., Métris, G., 1998. Symplectic mapping for satellites and space debris including nongravitational forces. Celestial Mech. Dyn. Astron. 71 (2), 79–94. https://doi.org/10.1023/a:1008356915763.

Breiter, S., Wytrzyszczak, I., Melendo, B., 2005. Long-term predictability of orbits around the geosynchronous altitude. Adv. Space Res. 35 (7), 1313–1317. https://doi.org/10.1016/j.asr.2005.02.033.

Brueck, H., 2018. NASA wants to send humans to Mars in the 2030s - here's the step-by-step timeline. URL: https://www.businessinsider.in/nasa-wants-to-send-humans-to-mars-in-the-2030s-heres-the-step-by-step-timeline/articleshow/63128425.cms Access Date: 26-01-2022.

Buinhas, L., Peytaví, G.G., Förstner, R., 2019. Navigation and communication network for the Valles Marineris Explorer (VaMEx). Acta Astronaut. 160, 280–296. https://doi.org/10.1016/j.actaastro.2019.04.032.

Chamberlin, A.B., 2019. Horizons system. URL: https://ssd.jpl.nasa.gov/?horizons Access Date: 18-06-2019.

Cintio, P.D., Rossi, A., Valsecchij, G.B., 217). Symplectic integrators for the simulation of space debris evolution. In: Proceedings of the International Astronautical Congress, IAC, vol. 1, pp. 267–273. paper number IAC-17, A6, IP,6, x39076. URL: https://iafastro.directory/iac/archive/browse/IAC-17/A6/IP/39076/.

Colombo, C., de Miguel, G.V., Skoulidou, D.K., Banos, N.M., Alessi, E. M., Gkolias, I., Carzana, L., Letterio, F., Schettino, G., Tsiganis, K., Rossi, A., 2019. Redshift disposal module for the design of end-of-life disposal trajectories for LEO to GEO missions. In: Proceedings of the International Astronautical Congress, IAC. volume 2019-October, paper number IAC-19, A6,6,4, x53705. URL: https://re.public.polimi.it/retrieve/handle/11311/1118894/462174/COLOC06-19.pdf.

Davis, D.C., Patterson, C., Howell, K., 2008. Solar gravity perturbations to facilitate long-term orbits: Application to Cassini. In: Advances in the Astronautical Sciences (pp. 383–401). volume 129 PART 1. URL: https://engineering.purdue.edu/people/kathleen.howell.1/Publications/Conferences/2007_AAS_DavPatHow.pdf.

Domínguez-González, R., Sánchez-Ortiz, N., Cacciatore, F., Radtke, J., Möckel, M., Flegel, S.K., Merz, K., 2013. Disposal strategies analysis for MEO orbits. In: Proceedings of the International Astronautical Congress, IAC (pp. 2061–2072). volume 3, paper number IAC-13, A6,2,5, x19061. URL: https://iafastro.directory/iac/archive/browse/IAC-13/A6/2/19061/.

Drake, N., 2016. Elon Musk: A million humans could live on Mars by the 2060s. URL: https://www.nationalgeographic.com/science/article/elon-musk-spacex-exploring-mars-planets-space-science Access Date: 26-01-2022.

ESA, 2019. Missions to Mars. URL: https://www.esa.int/spaceinimages/Images/2019/05/Missions_to_Mars Access Date: 10-06-2019.

Fecko, M., 2006. Differential Geometry and Lie Groups for Physicists. Cambridge University Press, Cambridge. https://doi.org/10.1017/CBO9780511755590.

Früh, C., Schildknecht, T., 2012. Variation of the area-to-mass ratio of high area-to-mass ratio space debris objects. Mon. Not. R. Astron. Soc. 419 (4), 3521–3528. https://doi.org/10.1111/j.1365-2966.2011.19990.x.

Gkolias, I., Colombo, C., 2019. Towards a sustainable exploitation of the geosynchronous orbital region. Celestial Mech. Dyn. Astron. 131 (4). https://doi.org/10.1007/s10569-019-9895-3, article number 19.

Hairer, E., Lubich, C., Wanner, G., 2006. Geometric Numerical Integration: Structure-Preserving Algorithms for Ordinary Differential Equations volume 31 of Springer Series in Computational Mathematics. Springer-Verlag, Berlin (Heidelberg). https://doi.org/10.1007/3-540-30666-8.

Hall, L., 2020. 6 technologies NASA is advancing to send humans to Mars. URL: https://www.nasa.gov/directorates/spacetech/6_Technologies_NASA_is_Advancing_to_Send_Humans_to_Mars Access Date: 26-01-2022.

Harwood, N.M., Swinerd, G.G., 1995. Long-periodic and secular perturbations to the orbits of Explorer 19 and Lageos due to direct solar radiation pressure. Celestial Mech. Dyn. Astron. 62 (1), 81–92. https://doi.org/10.1007/BF00692070.

Hofsteenge, R., 2013. Computational methods for the long-term propagation of space debris orbits. MSc Thesis, Delft University of Technology, Delft. URL: http://resolver.tudelft.nl/uuid:eee70164-4c99-470d-b8ee-5314ffcf63f8.

Hubaux, C., Lemaître, A., 2013. The impact of Earth's shadow on the long-term evolution of space debris. Celestial Mech. Dyn. Astron. 116 (1), 79–95. https://doi.org/10.1007/s10569-013-9480-0.

Hubaux, C., Lemaître, A., Delsate, N., Carletti, T., 2012. Symplectic integration of space debris motion considering several Earth's shadowing models. Adv. Space Res. 49 (10), 1472–1486. https://doi.org/10.1016/j.asr.2012.02.009.

Hubaux, C., Libert, A.S., Delsate, N., Carletti, T., 2013. Influence of Earth's shadowing effects on space debris stability. Adv. Space Res. 51 (1), 25–38. https://doi.org/10.1016/j.asr.2012.08.011.

Hughes, S., 1980. Earth satellite orbits with resonant lunisolar perturbations. i. resonances dependent only on inclination. Proc. Roy. Soc. London. Series A, Mathe. Phys. Sci. 372 (1749), 243–264. https://doi.org/10.1098/rspa.1980.0111.

Ineichen, D., Beutler, G., Hugentobler, U., 2003. Sensitivity of GPS and GLONASS orbits with respect to resonant geopotential parameters. J. Geodesy 77 (7), 478–486. https://doi.org/10.1007/s00190-003-0348-z.

ISRO, 2017. Mars Orbiter Mission completes 1000 days in orbit. URL: https://www.isro.gov.in/mars-orbiter-mission-completes-1000-days-orbit Access Date: 06-07-2019.

Jacobson, R.A., Lainey, V., 2014. Martian satellite orbits and ephemerides. Planet. Space Sci. 102, 35–44. https://doi.org/10.1016/j.pss.2013.06.003.

Jenkin, A.B., McVey, J.P., Sorge, M.E., Peterson, G.E., 2021. Search for long-term reentry disposal orbits across altitude and inclination. In 8th European Conference on Space Debris proceedings. volume 8, paper number 35. URL: https://conference.sdo.esoc.esa.int/proceedings/sdc8/paper/35/SDC8-paper35.pdf.

Johnson, Y., Engelhardt, R., 2018. Orbital Debris Assessment for the CubeSats on the ICESat-2/ELaNa-18 Mission per NASA-STD 8719.14A. Report. URL: https://apps.fcc.gov/els/GetAtt.html?id=211880&x=.

JPL (2006a). Mars Reconnaissance Orbiter - Fact sheet. URL: https://www.jpl.nasa.gov/news/fact_sheets/MRO.pdf Access Date: 06-07-2019.

JPL, 2006b. Mars Reconnaissance Orbiter arrival - Press kit. URL: https://www.jpl.nasa.gov/news/press_kits/mro-arrival.pdf Access Date: 06-07-2019.

Kaula, W., 1966. Theory of Satellite Geodesy: Applications of Satellites to Geodesy. Blaisdell Publishing Company, Bloomington (MN), URL: https://books.google.co.in/books?id=chNTnQEACAAJ.

Kelly, P.W., Bevilacqua, R., 2018. Constellation design for Mars navigation using small satellites. In: 2018 AIAA Aerospace Sciences Meeting proceedings. https://doi.org/10.2514/6.2018-1538 (Issue 210059, paper AIAA 2018-1538).

Kinoshita, H., Nakai, H., 1992. New methods for long-time numerical integration of planetary orbits. Symp. - Int. Astron. Union 152, 395–406. https://doi.org/10.1017/S0074180900091439.

Knapton, S., 2015. NASA planning 'Earth independent' Mars colony by 2030s. URL: https://www.telegraph.co.uk/science/2016/03/14/nasa-planning-earth-independent-mars-colony-by-2030s/ Access Date: 26-01-2022.

Kubo-oka, T., 1999. Long-term effect of solar radiation on the orbit of an octagonal satellite orbiting around the Moon. Adv. Space Res. 23 (4), 727–731. https://doi.org/10.1016/S0273-1177(99)00146-5.

Kuo, N.R., 2000. Mars network operations concept. In: 2000 IEEE Aerospace Conference proceedings (Cat. No.00TH8484), vol. 2. pp. 209–216. https://doi.org/10.1109/AERO.2000.878226.

Kuznetsov, E.D., Zakharova, P.E., Glamazda, D.V., Shagabutdinov, A. I., Kudryavtsev, S.O., 2012. Light pressure effect on the orbital evolution of objects moving in the neighborhood of low-order resonances. Sol. Syst. Res. 46 (6), 442–449. https://doi.org/10.1134/s0038094612050073.

Laskar, J., Robutel, P., 2001. High order symplectic integrators for perturbed hamiltonian systems. Celestial Mech. Dyn. Astron. 80 (1), 39–62. https://doi.org/10.1023/a:1012098603882.

Lemaître, A., 2019. Space debris: From LEO to GEO. In: G. Baú, A. Celletti, C.B. Galeş, G.F. Gronchi (Eds.), Satellite Dynamics and Space Missions. Springer International Publishing, Cham. pp. 115–157. https://doi.org/10.1007/978-3-030-20633-8_3.

Luo, X., Wang, Y., 2019. Luni-solar resonances and effect on long-term evolution of inclined geostationary transfer orbits. Acta Astronaut. 165, 158–166. https://doi.org/10.1016/j.actaastro.2019.09.005.

Luzum, B., Petit, G., 2012. The IERS conventions (2010): reference systems and new models. Proc. Int. Astron. Union 10 (H16), 227–228. https://doi.org/10.1017/S1743921314005535.

Lyons, D., Vaughn, R., 1999. Mars Pathfinder Project: Planetary constants and models. URL: http://hdl.handle.net/2014/16962 (Report presented at Mars Sample Return/CNES Coordination Meeting, Pasadena, California, USA on 03-03-1993) Access Date: 12-06-2019.

Menggen, S., Cui, P., Zhu, S., 2014. Networked Mars satellite system design and autonomous navigation analysis. In: The 26th Chinese Control and Decision Conference (2014 CCDC), pp. 3316–3321. https://doi.org/10.1109/CCDC.2014.6852747.

Montenbruck, O., Gill, E., 2000. Satellite Orbits: Models, Methods and Applications. Springer-Verlag, Berlin (Heidelberg). https://doi.org/10.1007/978-3-642-58351-3.

Mouret, S., Simon, J.L., Mignard, F., Hestroffer, D., 2009. The list of asteroids perturbing the Mars orbit to be seen during future space missions. A&A 508 (1), 479–489. https://doi.org/10.1051/0004-6361/200810979.

O'Keefe, K., Lachapelle, G., Skone, S., 2005. Assessing the global availability and reliability of the Mars network, a proposed global navigation satellite system for Mars. Ca. Aeronaut. Space J. 51 (1), 23–34. https://doi.org/10.5589/q05-003.

Pardini, C., Anselmo, L., 2012. Post-disposal orbital evolution of satellites and upper stages used by the GPS and GLONASS navigation constellations: The long-term impact on the medium Earth orbit environment. Acta Astronaut. 77, 109–117. https://doi.org/10.1016/j.actaastro.2012.03.024.

Rosengren, A.J., Skoulidou, D.K., Tsiganis, K., Voyatzis, G., 2019. Dynamical cartography of Earth satellite orbits. Adv. Space Res. 63 (1), 443–460. https://doi.org/10.1016/j.asr.2018.09.004.

Rossi, A., 2008. Resonant dynamics of medium Earth orbits: Space debris issues. Celestial Mech. Dyn. Astron. 100 (4), 267–286. https://doi.org/10.1007/s10569-008-9121-1.

Schettino, G., Alessi, E.M., Rossi, A., Valsecchi, G.B., 2019. Exploiting dynamical perturbations for the end-of-life disposal of spacecraft in LEO. Astro. Comput. 27, 1–10. https://doi.org/10.1016/j.ascom.2019.02.001.

Semenov, B.V., 2017. Reference frames. URL: https://naif.jpl.nasa.gov/pub/naif/toolkit_docs/C/req/frames.html Access Date: 10-12-2019.

Smith, D.E., Zuber, M.T., Torrence, M.H., Dunn, P.J., Neumann, G.A., Lemoine, F.G., Fricke, S.K., 2009. Time variations of Mars' gravitational field and seasonal changes in the masses of the polar ice caps. J. Geophys. Res.: Planets 114 (E5). https://doi.org/10.1029/2008JE003267, paper E05002.

Spaceflight101, 2019. MarCO – Mars Cube One. URL: http://spaceflight101.com/insight/marco/ Access Date: 06-07-2019.

SpaceX, 2019. Making life multiplanetary. URL: https://www.spacex.com/mars Access Date: 26-12-2019.

Suchantke, I., Soucek, A., Letizia, F., Braun, V., Krag, H., 2019. Space sustainability in Martian orbits - first insights in a technical and regulatory analysis. In: First International Orbital Debris Conference proceedings, p. no. 6110. URL: https://www.hou.usra.edu/meetings/orbitaldebris2019/orbital2019paper/pdf/6110.pdf.

Surovik, D., Scheeres, D., 2012. Computational efficiency of symplectic integrators for space debris orbit propagation. In: AIAA/AAS Astrodynamics Specialist Conference proceedings. https://doi.org/10.2514/6.2012-4744 (Paper AIAA 2012-4744).

Tingting, H., Xian, S., Nianchuan, J., Leewo, F., Jinsong, P., 2009. A preliminary designation of constellation distribution for Mars GNSS. In: 2009 15th Asia-Pacific Conference on Communications, pp. 306–309, article number 5375631. https://doi.org/10.1109/APCC.2009.5375631.

Tudat, 2018. TU Delft Astrodynamic Toolbox - Start Page. URL: http://tudat.tudelft.nl/ Access Date: 10-12-2019.

United Nations, 2019. Report of the Committee on the Peaceful Uses of Outer Space, sixty-second session, UN General Assembly, document A/74/20. URL: https://www.unoosa.org/res/oosadoc/data/documents/2019/a/a7420_0_html/V1906077.pdf Access Date: 26-01-2022.

Vallado, D.A., McClain, W.D., 2001. Fundamentals of Astrodynamics and Applications. Space Technology Library. Springer, Netherlands, URL: https://books.google.nl/books?id=PJLlWzMBKjkC.

Wakker, K.F., 2015. Fundamentals of astrodynamics. Delft University of Technology. TU Delft Library, Delft. URL: http://resolver.tudelft.nl/uuid:3fc91471-8e47-4215-af43-718740e6694e.

Wall, M., 2020. Colonizing Mars may require humanity to tweak its DNA. URL: https://www.space.com/mars-colony-human-genetic-engineering-tardigrades.html Access Date: 26-01-2022.

Wang, Y., Luo, X., Wu, X., 2020. Long-term evolution and lifetime analysis of geostationary transfer orbits with solar radiation pressure. Acta Astronaut. 175, 405–420. https://doi.org/10.1016/j.actaastro.2020.06.007.

Wytrzyszczak, I., Breiter, S., 2001. Long-term evolution of disposal orbits beyond the geostationary ring. Adv. Space Res. 28 (9), 1409–1414. https://doi.org/10.1016/S0273-1177(01)00447-1.

Zhao, Y., Gurfil, P., Zhang, S., 2017. Long-term orbital dynamics of smart dust. J. Spacecraft Rock. 55 (1), 125–142. https://doi.org/10.2514/1.A33854.

Zuber, M., 2008. Mars Reconnaissance Orbiter derived gravity data, NASA Planetary Data System, MRO-M-RSS-5-SDP-V1.0. URL: https://pds-geosciences.wustl.edu/mro/mro-m-rss-5-sdp-v1/mrors_1xxx/data/shadr/.